Journal of Materials Chemistry A

REVIEW

View Article Online
View Journal | View Issue

Cite this: J. Mater. Chem. A, 2019, 7, 23476

Block copolymer-based porous carbons for supercapacitors†

Tianyu Liu [a] and Guoliang Liu *[ab]

Porous carbons are promising materials for supercapacitor electrodes owing to their excellent electrical conductivity, high surface area, unique porous networks, and superior chemical inertness. This article summarizes the recent development of block copolymer-based porous carbons for supercapacitor electrodes. We first introduce the fundamentals of supercapacitors and block copolymers, followed by representative examples to highlight the use of block copolymers for fabricating porous carbons that have morphologies unattainable by other strategies. Instead of a comprehensive review, the article surveys papers published within the past five years. We discuss block copolymer-based porous carbons in the formats of zero-dimensional powders, one-dimensional fibers, two-dimensional films, and three-dimensional monoliths. In the end, the article presents a few challenges and opportunities associated with the application of block copolymers for supercapacitors.

Received 17th July 2019
Accepted 19th August 2019

DOI: 10.1039/c9ta07770g

rsc.li/materials-a

1. Introduction

The increasing demand for modern electronics calls for reliable and high-performance energy storage devices. Supercapacitors stand out owing to their ultrahigh power densities (>5000 W kg^{-1}) and ultralong lifetimes (millions of charge–discharge cycles).[1,2] An example application is ancillary power for electric vehicles that harvest energy from braking and provide boosts during start or acceleration.[3] Porous carbons are exceptional supercapacitor electrode materials because of their excellent electrical conductivity, large specific surface areas, outstanding structural tunability, and chemical inertness at room temperature.[4–6] Carbon materials store electrical energy mostly *via* electrical double layers (EDLs) at the electrode/electrolyte interfaces (Fig. 1a). An EDL consists of an inner Helmholtz

[a]Department of Chemistry, Virginia Tech, Blacksburg, VA 24061, USA. E-mail: gliu1@vt.edu

[b]Macromolecules Innovation Institute, Academy of Integrated Science-Division of Nanoscience, Virginia Tech, Blacksburg, VA 24061, USA

† Electronic supplementary information (ESI) available. See DOI: 10.1039/c9ta07770g

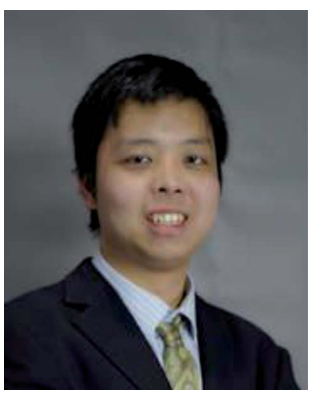

Dr. Tianyu Liu currently works as a postdoctoral associate in the Department of Chemistry, Virginia Tech. He obtained his PhD in Chemistry from the University of California, Santa Cruz (UCSC), USA in 2017, and received his B.S. in Chemistry from the University of Science and Technology, Beijing, China in 2012. His current research focuses on block copolymer-derived porous carbon materials for energy harvesting, conversion, and storage.

Dr. Guoliang Liu is an Assistant Professor of Chemistry, a courtesy Assistant Professor of Chemical Engineering, an affiliated professor of Macromolecules Innovation Institute, Virginia Tech Center for Sustainable Nanotechnology, and Academy of Integrated Science-Division of Nanoscience at Virginia Tech. Liu earned a bachelor's degree in chemical engineering from Zhejiang University, a doctorate degree in chemical engineering from the University of Wisconsin at Madison. He worked at HGST and conducted postdoctoral research at Northwestern University. Liu's research interests are in the areas of polymers and nanoparticles for energy and environmental sciences. His current focus is block copolymer-based porous carbon fibers.

layer (IHL) where ions distribute along the electrode surface to counter-balance surface charges, and an outer Helmholtz layer (OHL) of ions with charges opposite to those in the IHL. The charge-storage capacity of a carbon electrode, quantified by capacitance (C_{EDL}), is directly proportional to the ion-accessible surface area (S) of the electrode,

$$C_{EDL} = \frac{\varepsilon_0 \varepsilon_r S}{d} \quad (1)$$

where ε_0, ε_r, and d represent the vacuum permittivity (8.854×10^{-12} F m^{-1}), relative permittivity of electrolyte, and distance between ions in the IHL and charges on electrodes, respectively. For a given electrode–electrolyte system, ε_0, ε_r, and d are constant. Advanced EDL models (*e.g.*, Gouy–Chapman model[7]) present more accurate equations than eqn (1) for C_{EDL}, but the direct proportionality between C_{EDL} and S still holds. Therefore, porous carbons exhibit higher capacitances than their non-porous counterparts due mainly to the additional surface areas offered by the pores.

Rate capability, which measures how capacitance is retained at high discharge rates, is an important performance metric for energy storage devices. A high rate capability is indispensable for the high-power densities of supercapacitors. Electrode materials must respond timely to fast charging and discharging processes to achieve high rate capabilities, which demands low electrical resistance and fast ion diffusion kinetics. Because carbon materials generally have small electrical resistances, ion diffusion usually becomes the bottleneck and thwarts rate capabilities.[8,9] Quantitatively, the time (t) for a species with a diffusion coefficient D to diffuse a distance of L is

$$t = \frac{L^2}{qD} \quad (2)$$

where q is a dimensionality-dependent constant ($q = 2$, 4, or 6 for one-, two-, or three-dimensional diffusion, respectively). Meso and macro-pores in porous carbons could function as electrolyte reservoirs that hold ions close to electrode surfaces, which significantly reduces L, and therefore, shortens ion diffusion time and improves rate capability.[9]

Electrochemical cells (Fig. 1b and c) are often employed to evaluate the capacitances and rate capabilities of supercapacitors. The three-electrode testing configuration (Fig. 1b) probes the electrochemical performance of a single electrode. It consists of a working electrode containing the material of interest, a reference electrode providing a reference potential for the working electrode, and a counter electrode to complete the electric circuit. The two-electrode testing configuration (Fig. 1c) evaluates the performances of supercapacitor prototypes. This setup resembles an actual electrochemical device, with two electrodes—a positive electrode and a negative electrode—placed face to face in an electrolyte. Aqueous, organic solutions, and ionic liquids are the mostly used electrolytes.[10] Gel or solid electrolytes are for flexible or solid-state supercapacitors.[11]

This article presents the recent development of porous carbons derived from block copolymers for use in supercapacitor electrodes. Block copolymers are excellent in making porous carbons with tailorable morphologies and outstanding capacitive performances. We will discuss the versatile roles of block copolymers by introducing their self-assembly behaviors (Section 2) and the examples of block copolymer-based porous carbon electrodes (Section 3). Specifically, Section 3 is divided into three sub-sections according to the material dimensionalities, including zero-dimensional porous powders, one-dimensional fibers, two-dimensional films and sheets, and three-dimensional monoliths and aerogels. Each sub-section covers the syntheses, structures, and capacitive performances of the corresponding carbon materials. Two representative examples are given in each subsection for illustration. Lastly, we describe potential future directions and associated challenges of designing block copolymer-based porous carbon supercapacitor electrodes (Section 4).

2. Block copolymers

Homopolymers are polymers made of only one type of monomer. Differently, block copolymers are composed of two or more homopolymers covalently bonded together (Fig. 2a). Based on the numbers of the constituent blocks, linear block copolymers

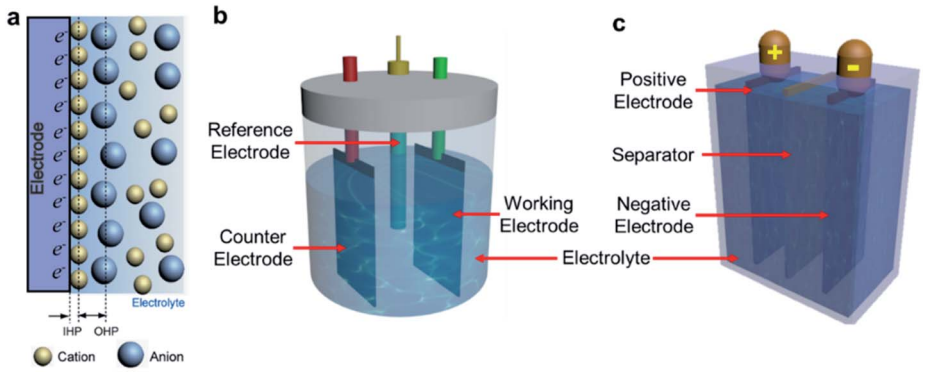

Fig. 1 Schematic illustrations of (a) an electrical double layer. IHP: inner Helmholtz layer; OHP: outer Helmholtz layer, (b) a three-electrode electrochemical cell, and (c) a two-electrode electrochemical cell. Panel (a) is reproduced with permission from ref. 9. Copyright 2017, Royal Society of Chemistry.

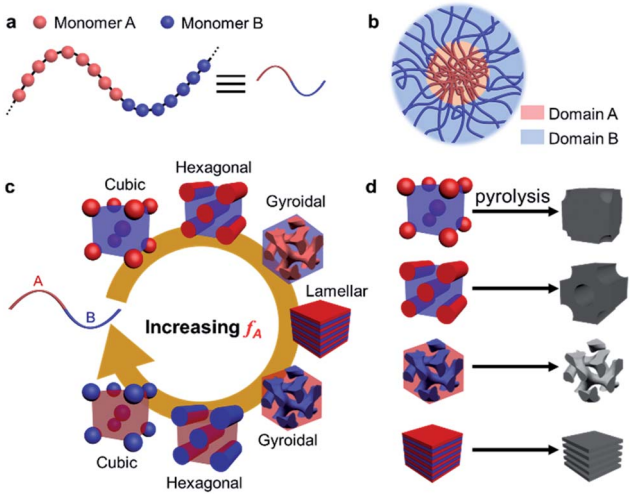

Fig. 2 (a) The structure of a linear di-block copolymer. (b) A core–shell micelle formed by linear di-block copolymers. (c) Increasing the volumetric fraction of one block (f_A) in a di-block copolymer results in morphologies such as cubic spheres, hexagonally packed cylinders, gyroids, and lamellae. (d) Examples of porous carbon structures after pyrolysis of block copolymers. The red and blue domains are sacrificial and carbon-generating blocks, respectively.

are categorized into di-block copolymers, tri-block copolymers, and multi-block copolymers.[12] Block copolymers are usually synthesized by polymerizing one block, followed by growing additional blocks from the reactive end(s) of pre-synthesized block(s). Widely practiced synthesis methods of block copolymers include atom transfer radical polymerization (ATRP),[13] reversible addition fragmentation chain transfer (RAFT) polymerization,[14] living cationic/anionic polymerization,[15,16] and ring-opening metathesis polymerization (ROMP).[17]

The renowned characteristics of block copolymers are their capability of nanoscale phase-separation and self-assembly into thermodynamically equilibrated morphologies. Because the constituent polymers are immiscible, polymer blocks of identical compositions aggregate and repel the foreign blocks if given sufficient energy and repulsion force, leading to distinct mesoscale structures such as core–shell micelles (Fig. 2b). Three factors determine the self-assembled morphologies, including the dimensionless Flory–Huggins interaction parameter (χ) correlating with the free-energy cost per monomer upon mixing different blocks, total degree of polymerization (or molecular weight) (N), and volumetric fraction of one block (f_i).[12] For A–B di-block copolymers, when the product of χ and N exceeds a threshold value (the so-called order–disorder transition (ODT) limit), they self-assemble into cubic (or spherical), hexagonal, gyroidal, and lamellar structures depending on f_A (Fig. 2c). Tri-block or multi-block copolymers form more complicated morphologies than di-block copolymers.[18]

Block copolymers are versatile precursors for generating porous carbons. For example, in a di-block copolymer, if one block has a high carbon yield or is infiltrated with precursors of high carbon yields (blue blocks in Fig. 2d) and the other block is thermally volatile (red blocks in Fig. 2d), after pyrolysis the block copolymers generate porous carbons replicating the self-assembled mesoscale structures (Fig. 2d). The domain sizes are tunable by the block copolymer molecular weight,[19–21] solvents used in solvent annealing,[22] and pyrolysis temperatures.[22–24] Because the sizes of the block copolymer domains are on the mesoscale, the pores after pyrolysis are dominantly mesopores. These mesopores, together with micropores that can be created by physical and chemical activation,[25] and macropores from templating methods,[26] macro-phase separation,[27] and 3D printing,[28] collectively build hierarchically porous networks that bestow ultrahigh surface areas and ultralow ion diffusion resistances.

3. Block copolymer-based porous carbon electrodes

3.1 Zero-dimensional porous carbon powders

Zero-dimensional porous carbon powders are facilely produced from block copolymers because block copolymers are often prepared in powders. In the context of porous carbons, block copolymers are either employed as sacrificial templates for pore generation (the so-called "soft-template" method) or directly carbonized into porous carbons.

Pluronic F127 is a widely used block-copolymer template for making porous carbon powders. It is a hydrophilic, non-ionic surfactant composed of a middle hydrophobic polypropylene oxide (PPO) block (~56 kDa) and two hydrophilic polyethylene oxide (PEO) flank blocks (~101 kDa each). Because Pluronic F127 has a low carbon yield, it is often blended with synthetic carbon precursors such as phenolic resin,[29–34] resorcinol resin,[35] melamine-formaldehyde resin,[36] *m*-aminophenol,[37] and polypyrrole,[38] or natural carbon precursors such as lignin,[39] starch,[40] and fructose.[41,42] Upon mixing, Pluronic F127 self-assembles into nanostructures together with the carbon-precursors. Subsequent pyrolysis removes Pluronic F127 and leaves behind uniform and closely packed mesopores.

Because Pluronic F127 offers limited tunability in pore size and pore arrangement, researchers have used other block copolymers such as polystyrene-*block*-polyethylene oxide (PS-*b*-PEO)[43–45] and polystyrene-*block*-poly(4-vinyl pyridine) (PS-*b*-P4VP)[46] to tune the porous structures. An example is hollow carbon nano-bowls derived from PS-*b*-PEO (Fig. 3).[43] In a mixed solvent of dioxane and water, PS-*b*-PEO self-assembled into collapsed vesicles (Kippah vesicles) comprising PEO coronas and PS walls (Fig. 3a). Afterward, dopamine was polymerized to form a uniform coating of polydopamine on the surfaces of the vesicles. After pyrolysis at 900 °C, the carbonization of polydopamine and the removal of PS-*b*-PEO resulted in hollow bowl-shaped carbon particles with a wall thickness of 20–30 nm (Fig. 3b and c). Compared with spherical analogs, the bowl-shaped particles showed reduced electrical contact resistance due to the large contact areas with adjacent particles. Additionally, the hollow structure with porous walls enlarged the ion-accessible surface area and facilitated ion diffusion. As a result, the hollow bowl-shaped carbon particles exhibited a gravimetric capacitance approaching 200 F g^{-1} at 10 A g^{-1},

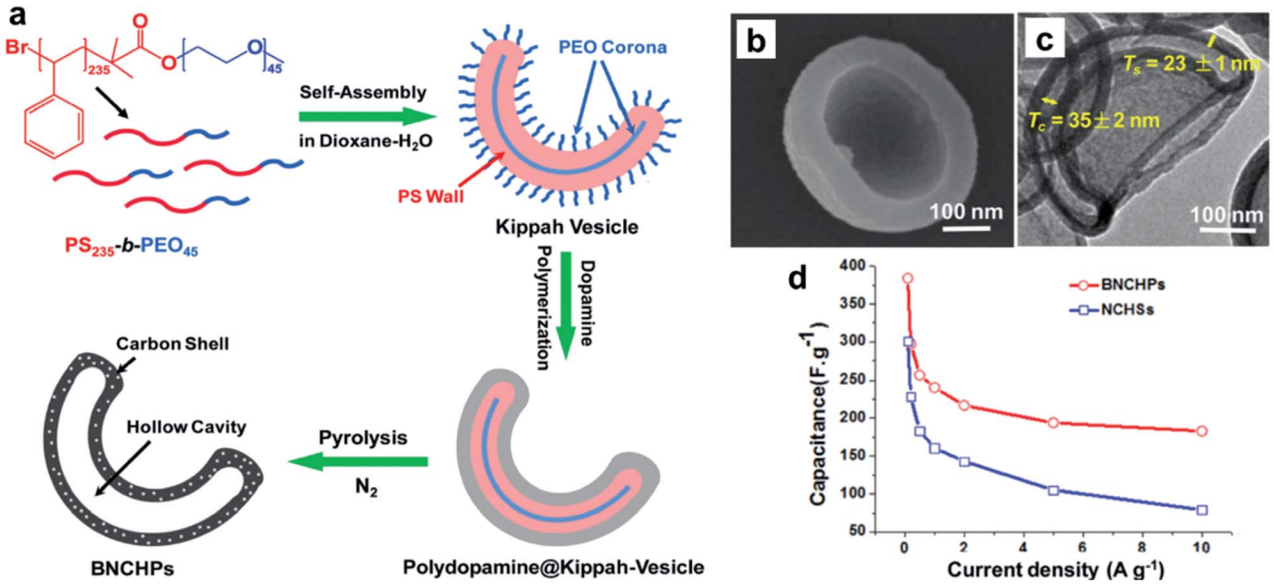

Fig. 3 (a) Synthesis of bowl-shaped, nitrogen-doped carbon hollow particles (BNCHPs) from polydopamine using a PS-*b*-PEO template. (b) SEM and (c) TEM images of a representative BNCHP. T_s and T_c are the thicknesses of the shell and core, respectively. (d) Rate capabilities of BNCHP and nitrogen-doped hollow carbon spheres (NCHs). Reproduced with permission from ref. 43. Copyright 2016, Royal Society of Chemistry.

more than three times higher than that of hollow carbon spheres at identical current density (Fig. 3d).

Direct synthesis of porous carbons from block copolymers is efficient because it eliminates the steps of dispersing and removing templates. To be suitable carbon precursors, block copolymers must consist of a polymer block with a high carbon yield, for example, polyacrylonitrile (PAN)[19,20,23,47–50] and polyimides.[51,52] These high carbon-yield polymers are coupled with sacrificial polymers that decompose at elevated temperatures, such as poly(*n*-butyl acrylate) (PBA),[19,47] poly(methyl methacrylate) (PMMA),[20,48,49] and PS.[23,50,53] For example, Kowalewski, Matyjaszewski, and co-workers demonstrated a sulfur-stabilization approach to synthesize N/S co-doped mesoporous carbon powders from PAN-*b*-PBA.[47] A critical step to ensure a high carbon yield is to stabilize PAN at temperatures ranging from 150 to 400 °C in an oxygen-containing atmosphere. The stabilization step cyclizes and crosslinks PAN chains; however, it partially degrades the sacrificial blocks and damages the porous structures of carbon powders. The authors re-designed the stabilization step by switching the stabilizing agent from oxygen to sulfur (Fig. 4a). In comparison with air-stabilized PAN-*b*-PBA ($CTNC_O$), the sulfur-stabilized PAN-*b*-PBA ($CTNC_S$) produced carbons containing well-resolved mesopores (Fig. 4b) with a narrower pore size distribution (Fig. 4c), owing to the coordination between sulfur and PBA that preserved the phase-separated domains during oxidation. Ultimately, the N/S co-dopants and well-developed mesopores offered $CTNC_S$ a high gravimetric capacitance of 236 F g^{-1} at 0.1 A g^{-1} (Fig. 4d).

3.2 One-dimensional porous carbon fibers

Carbon fibers are promising electrode materials for portable and wearable supercapacitors. Compared to zero-dimensional particles, one-dimensional fibers provide continuous electron conduction pathways with a small electrical resistance. Additionally, the ultrahigh aspect ratio (length to diameter) of carbon fibers provides a large ion-accessible surface area and reduces the ion diffusion distance; the latter is critical for high rate capabilities. Moreover, carbon fibers are weavable into fabrics, allowing for uses in smart textiles and wearable electronics.[54]

Block copolymer-based porous carbon fibers strengthen the inherent advantages of carbon fibers by introducing additional surface areas from microphase separation and improving ion diffusion kinetics. Typically, block copolymers are first made into polymer fibers[55–59] by solution spinning,[60] melt spinning,[61] and electrospinning.[62] By drawing charged polymer solutions into fine threads under a high voltage, electrospinning is the most widely adopted method for synthesizing block copolymer fibers. The polymer fibers are then carbonized into porous carbon fibers.

Our group has demonstrated the use of poly(methyl methacrylate)-*block*-polyacrylonitrile (PMMA-*b*-PAN) to create porous carbon fibers (PCFs) with highly uniform mesopores interconnected with micropores. The porous carbon fibers are directly used as high-performance supercapacitor electrodes[56] or as highly conductive supports for pseudocapacitive materials such as manganese dioxide (MnO_2).[57] Taking advantage of the microphase-separation between PMMA and PAN [Fig. 5a(1 and 2)], the PCFs possessed uniform mesopores interconnected with micropores in a continuous carbon fiber network (Fig. 5b). Impressively, the uniform mesopores supported a large amount of MnO_2 without clogging the ion diffusion [Fig. 5a(3)], ensuring effective and efficient ion transport within the porous carbon network. A large surface area of >500 m^2 g^{-1} and rich dopants of nitrogen and oxygen inherited from PAN

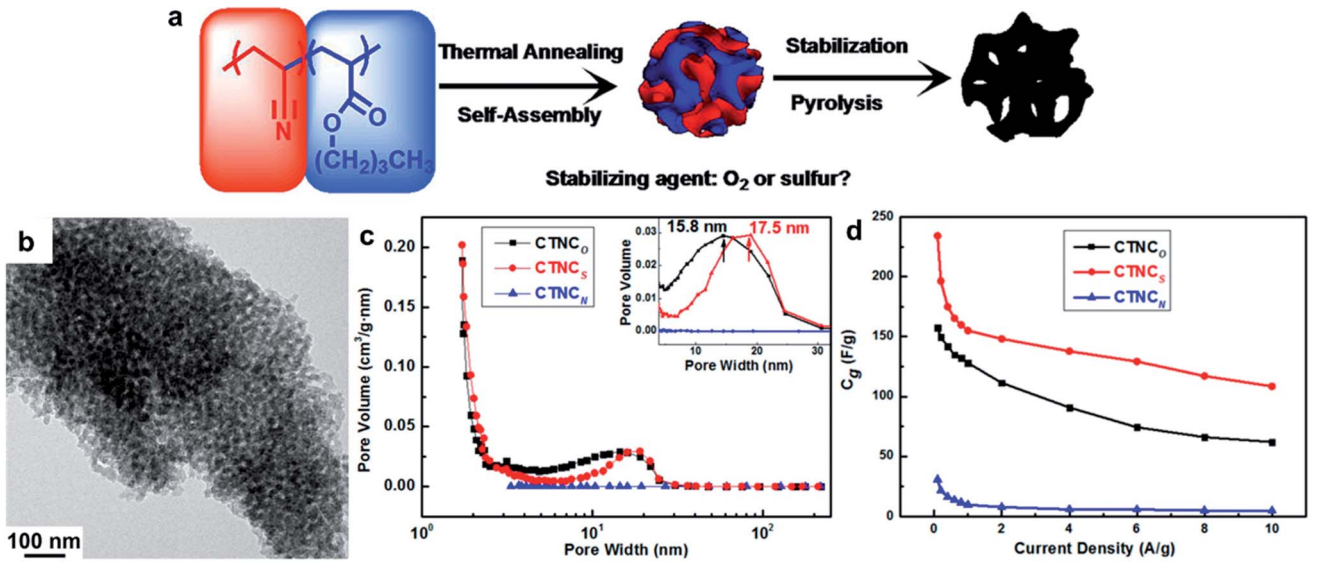

Fig. 4 (a) Synthesis of porous carbon powders from O_2- or S-stabilized PAN-*b*-PBA ($CTNC_O$ or $CTNC_S$). (b) TEM image of a mesoporous $CTNC_S$ particle. (c) Pore size distributions of $CTNC_O$, $CTNC_S$, and porous carbon powders from N_2-stabilized PAN-*b*-PBA ($CTNC_N$). Because PAN cannot be adequately stabilized under N_2, pore collapsed and $CTNC_N$ showed little pore volume. (d) Rate capabilities of $CTNC_O$, $CTNC_S$, and $CTNC_N$ in 6 M aqueous KOH solutions. Reproduced with permission from ref. 47. Copyright 2019, American Chemical Society.

stabilization contributed to a high specific capacitance of 360 F g^{-1} at 1 A g^{-1}, which surpassed the state-of-the-art carbon fibers with comparable or higher surface areas (Fig. 5c). The PCF-supported MnO_2 electrodes (PCF@MnO_2) reached a high mass loading approaching 7 mg cm^{-2} (Fig. 5d). After loading MnO_2, the electrode still retained unclogged mesopores to facilitate ion diffusion and achieved outstanding gravimetric and areal capacitances superior to recently reported MnO_2-based electrodes with various mass loadings (Fig. 5e).

Besides electrospinning, Kang *et al.* utilized a hard-template method to fabricate self-standing porous carbon fibers from PS-*b*-PEO (Fig. 6a).[63] They blended resol (a carbon precursor) with PS-*b*-PEO and infiltrated them into vertically aligned macropores of a piece of anodized aluminum oxide (AAO) film. After pyrolysis of the polymers and removal of the AAO template, the resol-containing PS-*b*-PEO generated self-standing ordered mesoporous carbon fiber arrays (OMC-NA) (Fig. 6b). The uniform mesopores resulted from the gasification of PS-*b*-PEO (Fig. 6c). N_2-physisorption revealed that the pore size was narrowly distributed and showed a peak at ~30 nm. The aligned carbon fiber arrays and uniform mesopores in each fiber facilitated electron conduction and ion diffusion. At current densities higher than 10 A g^{-1}, OMC-NA exhibited gravimetric capacitances more than four times those of porous carbon powders (OMC-BP) and nearly twice those of unsupported porous carbon fibers (OMC-BW) (Fig. 6e).

3.3 Two-dimensional porous carbon films and sheets

The capacitive performances of two-dimensional sheets are often compromised by the aggregation between adjacent layers and the impeded ion diffusion in the out-of-the-plane direction. Creating pores penetrating these sheets is an efficient method to avoid the drawbacks. Sheet-penetrating pores open the diffusion channels among neighbouring layers and thus significantly speed up the ion diffusion.[70] This method has been effective in ensuring fast-charging capability and ultrahigh power density.

Depositing block copolymers on two-dimensional substrates is a common strategy to synthesize porous carbon sheets. For example, graphene oxide (GO) is adopted as a substrate because of its two-dimensional nature and rich surface oxygen-functionalities to firmly anchor block copolymers.[71–73] Upon pyrolysis, the GO templates are reduced to electrically conductive reduced graphene oxide (rGO) sheets that support the block copolymer-derived porous carbon films. These porous carbon sheets are typically sub-nm thick and tend to self-stack, which reduces their ion-accessible surface areas. To mitigate this problem, Xi *et al.* chose MgAl-layered double hydroxide (LDH) sheets with a relatively large thickness of 10 nm and weak inter-sheet interactions (Fig. 7a).[74] They first assembled resol-infiltrated Pluronic F127 micelles onto the basal planes of the LDH nanosheets and then crosslinked the resols *via* a hydrothermal reaction. Afterward, the crosslinked resol/LDH sheets were carbonized at 700 °C under N_2 and washed with acid to dissolve the LDH sheets. The resultant carbon sheets exhibited hexagonally packed mesopores (Fig. 7b) and showed promising capacitive behaviors, as reflected by their quasi-rectangular cyclic voltammograms across a broad range of scan rates from 30 to 3000 mV s^{-1} (Fig. 7c).

Template-free methods, including solution casting,[22,75–77] flow casting,[78] and spin coating,[79] are powerful for fabricating block copolymer-based porous carbon sheets. Generally, these methods spread block copolymer solutions onto flat substrates and rapidly remove the solvents to form thin films. For example, our group demonstrated a solution cast method of PMMA-*b*-PAN thin films

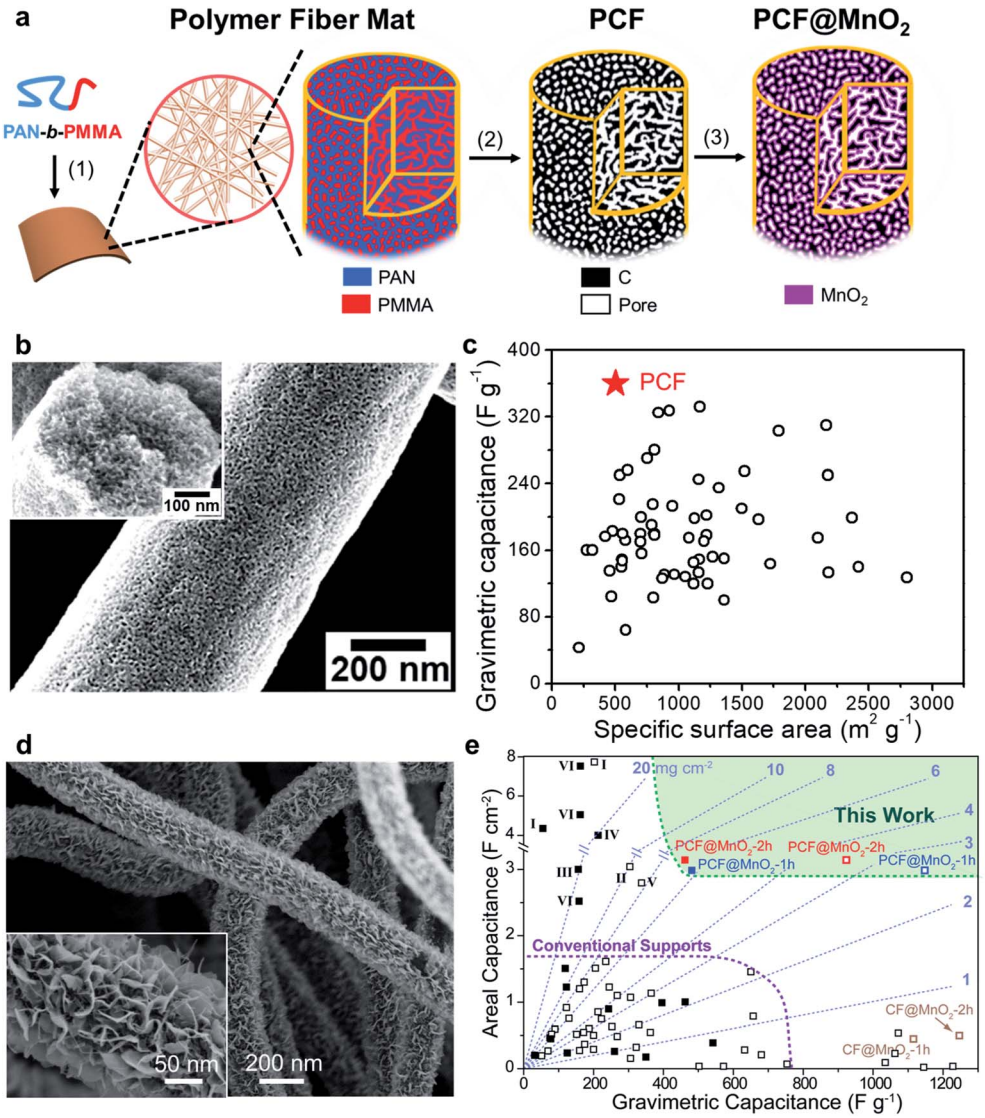

Fig. 5 (a) Synthesis of PMMA-*b*-PAN based porous carbon fibers (PCFs) and MnO_2-coated PCFs (PCF@MnO_2). PMMA-*b*-PAN was first electrospun into block copolymer fibers (1), thermally annealed to trigger the self-assembly into bi-continuous interpenetrating PMMA (red) and PAN (blue) domains (2), pyrolyzed to PCFs (3), and soaked in $KMnO_4$ aqueous solutions to deposit MnO_2 on the surfaces and inside pores (4). (b) SEM images of PCFs showing the uniform mesopores on the fiber surface. (Inset) A cross-section SEM image showing the interconnected pores inside the fiber. (c) The gravimetric capacitance and specific surface area of PCFs in comparison with those of state-of-the-art porous carbon fiber electrodes. (d) SEM images of PCF@MnO_2. (Inset) A high-magnification SEM image highlighting the MnO_2 nanosheets on PCF. (e) Comparison of areal capacitances and gravimetric capacitances of PCF@MnO_2 with state-of-the-art porous carbon-MnO_2 composite electrodes. (I) wood-derived porous carbon@MnO_2;[64] (II) hierarchical MnO_2 on carbon cloth;[65] (III) carbon nanotube (CNT)@MnO_2;[66] (IV) activated carbon-coated CNT@MnO_2;[67] (V) CNT-wrapped polyester fiber@MnO_2;[68] (VI) carbon nanofoam@MnO_2.[69] Open and solid squares represent capacitance based on entire masses and MnO_2 masses, respectively. Panels (a), (d), and (e) are reproduced with permission from ref. 57. Copyright 2019, Springer Nature. Panels (b) and (c) are reproduced with permission from ref. 56. Copyright 2019, American Association for the Advancement of Science.

and thermally pyrolyzed them into mesoporous carbon films with controllable pore sizes and pore-to-pore distances.[22]

Ran *et al.* spin-coated a polymer blend of PAN-*b*-PMMA-*b*-PAN and PAN in *N*,*N*-dimethyl formaldehyde (DMF) (Fig. 8a). The as-coated films were immediately submerged in a coagulation bath of distilled water to solidify the film. Carbonization of the solidified film followed by nitric acid corrosion generated a porous carbon film. The macropores in the cross-sectional SEM were induced by coagulation (Fig. 8b), and the abundant mesopores were caused by the microphase separation of PAN-*b*-PMMA-*b*-PAN (Fig. 8c). The surface area and pore volume of the porous carbon films peaked at 5 wt% of PAN-*b*-PMMA-*b*-PAN, resulting in a high specific capacitance and rate capability (Fig. 8d).

3.4 Three-dimensional porous carbon monoliths and aerogels

Three-dimensional porous carbons are suitable for high-power electrochemical energy storage because their three-dimensional hierarchically porous networks provide large ion-accessible

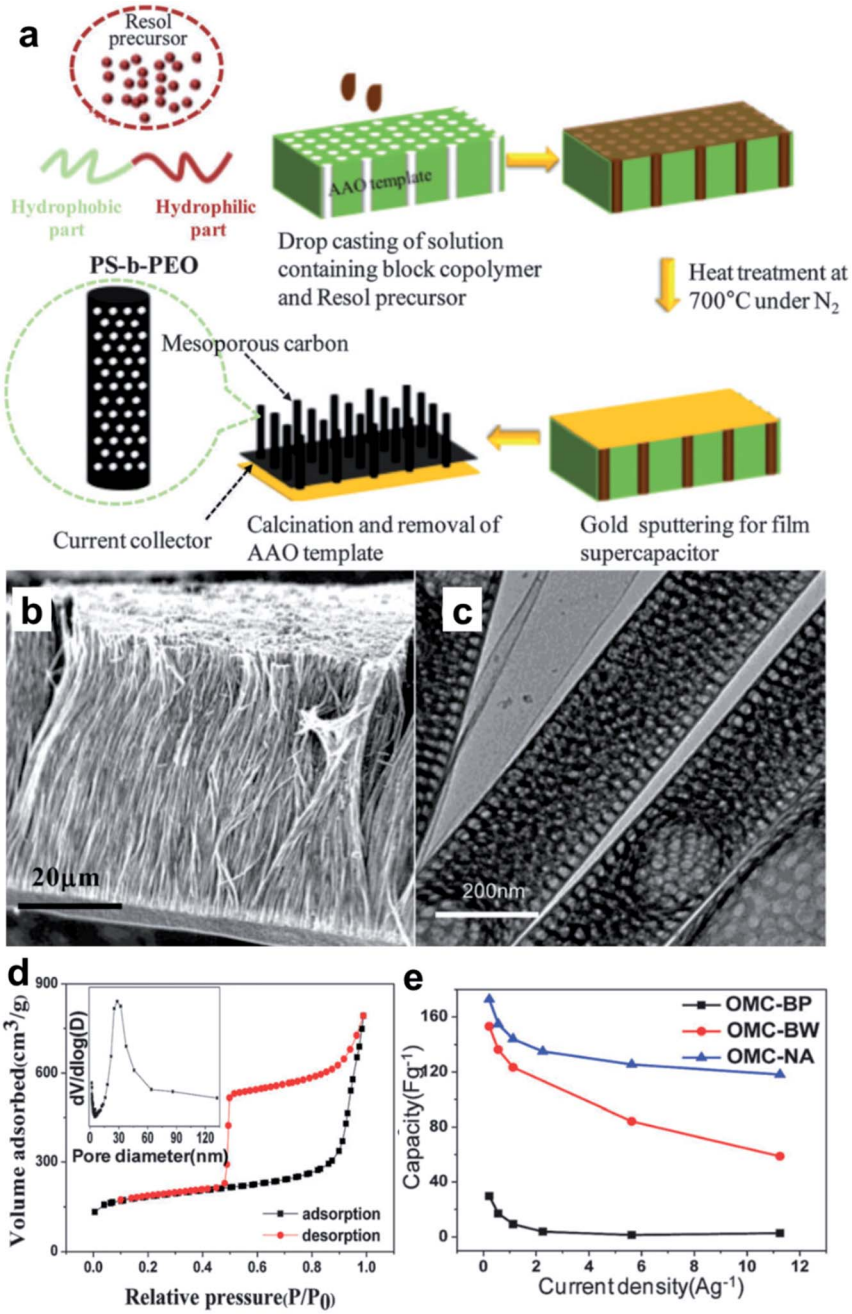

Fig. 6 (a) Synthesis of ordered mesoporous carbon fiber arrays (OMC-NA) from resol-infiltrated PS-*b*-PEO confined in an anodic aluminum oxide (AAO) template. The carbon arrays were supported on a gold film. (b) SEM image of OMC-NA. (c) TEM image of representative mesoporous carbon fibers. (d) N_2-physisorption isotherm of OMC-NA at 77 K. (Inset) The pore size distribution of OMC-NA. (e) Gravimetric capacitances of OMC-NA at various current densities, in comparison with unsupported mesoporous carbon fibers (OMC-BW) and mesoporous carbon powder (OMC-BP) in a 2 M aqueous H_2SO_4 electrolyte. Reproduced with permission from ref. 63. Copyright 2013, Royal Society of Chemistry.

surface areas and small ion diffusion resistances. Block copolymer-based three-dimensional porous carbons are primarily derived by carbonization of organic matrices embedded with Pluronic block copolymers, *e.g.*, F127 (PEO_{106}-*b*-PPO_{70}-*b*-PEO_{106}),[80–87] F68 (PEO_{76}-*b*-PPO_{29}-*b*-PEO_{76}),[88] and P123 (PEO_{20}-*b*-PPO_{70}-*b*-PEO_{20}).[85] Other thermally liable block copolymers such as polystyrene-*block*-poly(acrylic acid) (PS-*b*-PAA)[89] are occasionally used. The carbon precursors are mostly phenolic resins,[80–82,88] carbides,[86] and GO sheets.[83,87] Other heteroatom-rich organic compounds, such as urea-formaldehyde resins,[89] dicyandiamide,[85] 2-thiophenecarboxaldehyde,[80] cysteine,[87] polydopamine,[87] and melamine,[88] have been blended with carbon precursors to introduce heteroatoms into the carbon matrices. These dopants give rise to pseudocapacitance and accelerate electron transfer at electrode–electrolyte interfaces.

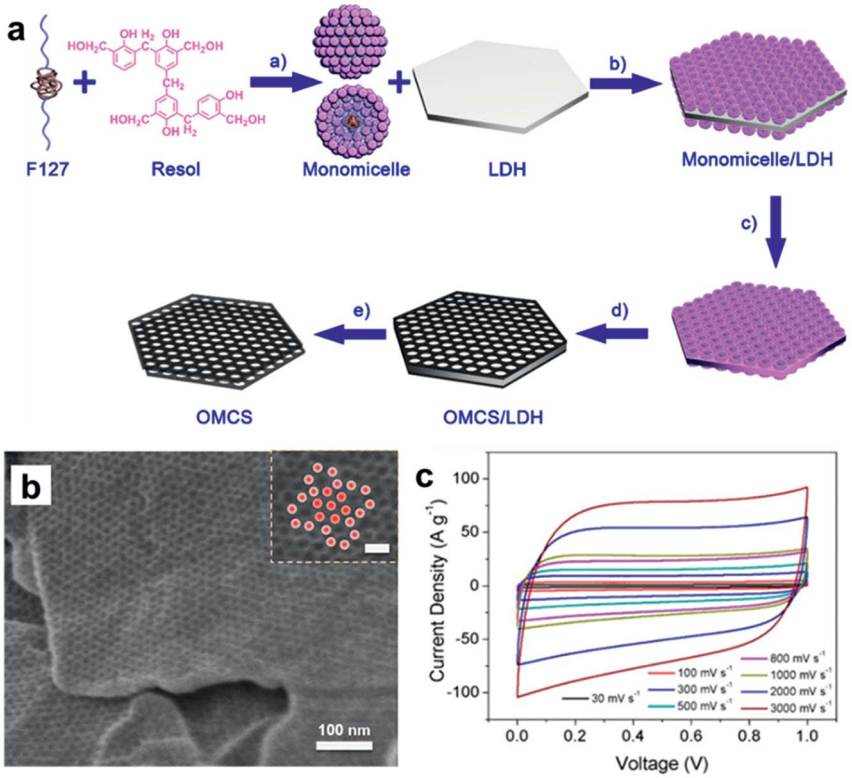

Fig. 7 (a) Synthesis of ordered mesoporous carbon sheets (OMCS) from resol-infiltrated Pluronic F127 and MgAl-layered double hydroxide (LDH) sheet templates. (b) SEM image of OMCS. (Inset) The hexagonal pattern of Pluronic F127-induced mesopores. Scale bar: 25 nm. (c) Cyclic voltammograms of OMCS at scan rates from 30 mV s^{-1} to 3000 mV s^{-1}. Reproduced with permission from ref. 74. Copyright 2018, American Chemical Society.

Block copolymers are used in conjunction with hard-templates (*e.g.*, titanium dioxide[85] and silica[81,83]), poor solvent-induced phase separation[84] or post-pyrolysis activations[87,88] to obtain three-dimensional multiscale hierarchically porous structures. For example, Peng *et al.* reported a three-dimensional graphene aerogel with uniform mesopores

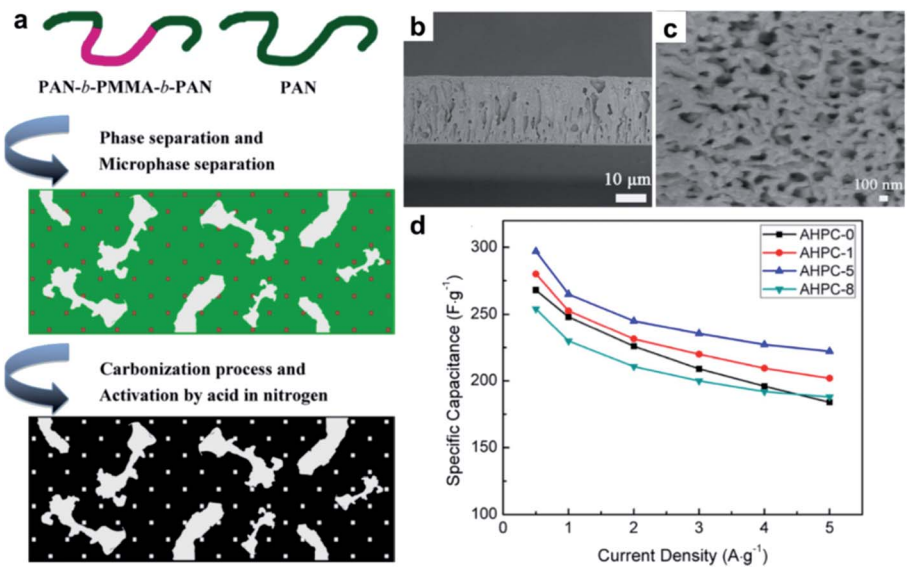

Fig. 8 (a) Synthesis of activated hierarchical porous carbon (AHPC) from a blend of PAN-*b*-PMMA-*b*-PAN (0–8 wt%) and PAN (15 wt%). (b) Side-view and (c) top-down SEM images of AHPC-5 ("5" denotes the mass percentage of the block copolymer in wt%). (d) Rate capabilities of various AHPC electrodes (AHPC-*x*, *x* represents the mass percentage of the block copolymer in wt%) in a 1 M aqueous Na_2SO_4 electrolyte. Reproduced with permission from ref. 79. Copyright 2016, Elsevier.

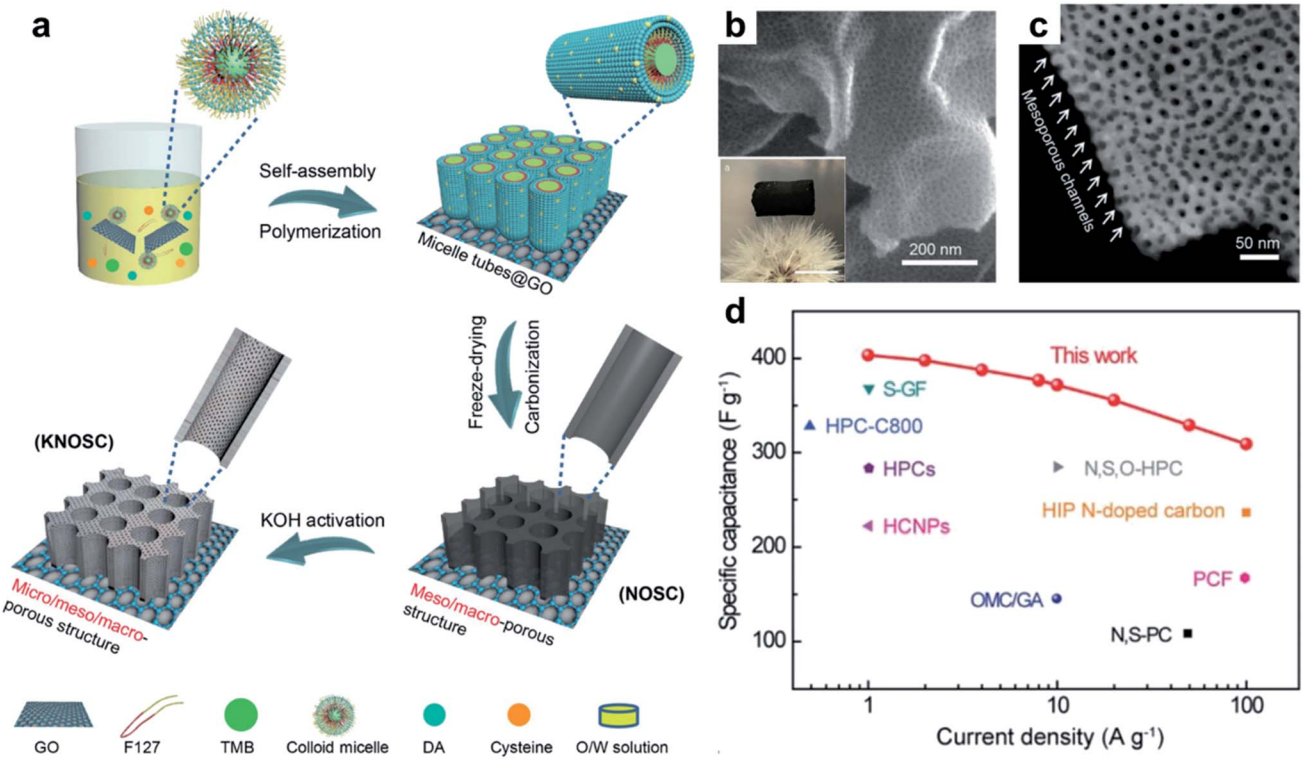

Fig. 9 (a) Synthesis of KOH activated, N/O/S tri-doped hierarchical porous carbon/graphene aerogels (KNOSC) from Pluronic F127 containing dopamine and cysteine. (b and c) SEM images of KNOSC highlighting (b) uniform mesoporous surfaces and (c) penetrating mesopores in a piece of KNOSC sheet. (Inset) A photograph showing the lightweight feature of KNOSC. (d) The rate capability of KNOSC in comparison with other state-of-the-art porous carbon electrodes. Reproduced with permission from ref. 87. Copyright 2019, Wiley Publishing Group.

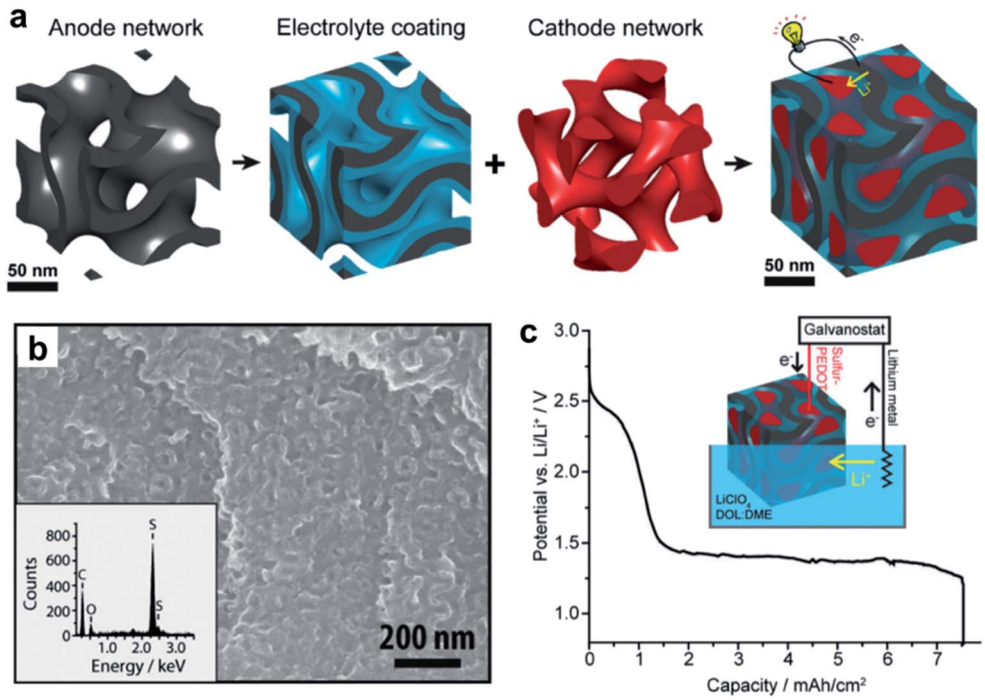

Fig. 10 (a) Schematics of sequential assembly of a three-dimensional energy-storage device based on a piece of double gyroidal carbon from polyisoprene-*block*-polystyrene-*block*-polyethylene oxide (PIO-*b*-PS-*b*-PEO) infiltrated with phenol-formaldehyde resols. Black: carbon (anode); blue: poly(phenylene oxide) (electrolyte); red: sulfur blended with poly(3,4-ethylene dioxythiophene) (cathode). (b) SEM image of the assembled device. (Inset) Elemental mapping of the imaged region. (c) A discharge profile (potential *vs.* capacity) of the assembled device upon lithiation in an organic electrolyte ($LiClO_4$ in 1,3-dioxolane and dimethoxyethane). Reproduced with permission from ref. 90. Copyright 2018, Royal Society of Chemistry.

created by a solution assembly strategy (Fig. 9a).[87] First, Pluronic F127 micelles coated with polydopamine and cysteine were deposited onto sheets of graphene oxide (GO) hydrogel. Afterward, freeze-drying and carbonization converted the GO hydrogels into reduced graphene oxide aerogels possessing oxygen (from GO), nitrogen (from polydopamine) and sulfur (from cysteine) heteroatoms. Finally, the aerogels were activated by KOH to create micropores. SEM images showed that each graphene sheet contained uniform and penetrating mesopores derived from Pluronic F127 (Fig. 9b and c). The mesoporous graphene aerogel delivered a high gravimetric capacitance of $\sim$400 F g^{-1} at 1 A g^{-1} and retained $\sim$300 F g^{-1} when the current density increased by 100 times (Fig. 9d). The excellent rate capability is mainly correlated with three factors: (1) an ultrahigh surface area of 2685 m^2 g^{-1} to form electrical double layers; (2) a three-dimensional hierarchical porous network involving micropores, mesopores, and inter-sheet macropores to facilitate ion diffusion; (3) rich heteroatoms to enhance electrolyte affinity and contribute pseudocapacitance.

Block copolymer-derived three-dimensional mesoscale structures are promising nano-sized energy storage devices, as demonstrated by Wiesner and co-workers.[90] Although the device is strictly not a supercapacitor, it is an excellent example of block copolymer design for energy storage and adaptable into supercapacitors. The authors first synthesized a gyroidal carbon anode from poly(isoprene)-*block*-poly(styrene)-*block*-poly(ethylene oxide) (PIO-*b*-PS-*b*-PEO) infiltrated with phenol-formaldehyde resols. Then, they filled the porous anode with a poly(phenylene oxide) polyelectrolyte and a sulfur-blended poly(3,4-ethylene dioxythiophene) cathode (Fig. 10a). The interpenetrating anode/electrolyte/cathode configuration dramatically decreased the anode-to-cathode distance (Fig. 10b), which increased the ion diffusion rate and the packing density of active materials. Electrochemical tests showed that the nanosized device could store lithium ions with a stable voltage plateau of $\sim$1.4 V *vs.* Li^+/Li and an areal capacity of 7.5 mA h cm^{-2} (Fig. 10c).

4. Conclusions and outlooks

We herein highlight examples of block copolymer-based porous carbons for uses in supercapacitor electrodes. The literature survey is based on the dimensionality of carbon. In all cases, block copolymers are versatile materials as pore templates or directly as carbon precursors. The capacitive performances (gravimetric capacitance, rate capability, and cycling stability) of the carbons discussed in this article are summarized in Table S1 (ESI†). With the increasing need for energy storage, block copolymers will continue to play an important role in advancing the science of energy storage. Projecting forward, there are numerous opportunities and challenges associated with applying block copolymer-based porous carbon electrodes in supercapacitors.

First, block copolymer-based porous carbons are integrable with pseudocapacitive materials to boost the capacitances and energy densities. Pseudocapacitive metal oxides have inherently higher capacitance than electrical double layer capacitive carbons but are usually electrically insulating and unstable after extensive charge and discharge cycles. Integrating pseudocapacitive materials with carbon that is electrically conductive and electrochemically stable can mitigate these drawbacks. Introducing pseudocapacitive materials or their precursors into block copolymers is an attractive integration method, but one must be meticulous in preventing the guest materials from interfering block copolymer self-assembly. Alternatively, pseudocapacitive materials can be directly deposited onto the carbon matrices, but the mass loadings of the pseudocapacitive materials must be tailored to ensure uniform deposition and prevent pore blockage. Pseudocapacitance can also be provided by heteroatoms (*e.g.*, nitrogen and oxygen) from the carbon precursors, for instance, melamine with 66.6 wt% of nitrogen. The temperature and time of the pyrolysis step must be optimized because they strongly affect the concentrations of heteroatoms in the resultant carbons.[24,91]

Second, it is full of potential, yet challenging, to employ delicate structures of multi-block copolymers in supercapacitors. Because a typical supercapacitor has at least two electrodes and an electrolyte, it is possible to directly engineer the three blocks of tri-block copolymers into the three components of a supercapacitor. Such supercapacitors with nanoscale and inter-penetrating electrodes can potentially exhibit high areal and volumetric capacitances. Constructing nanoscale supercapacitors from block copolymers demands high-quality block copolymers to ensure excellent resolution of their self-assembled structures. Synthesis methods of such block copolymers could be developed from protocols of commercial multi-block copolymers (*e.g.*, Pluronic F127).

Third, direct pyrolysis of block copolymers into porous carbons is facile in producing supercapacitor electrodes, but the structures are mainly limited to disordered pores and may have high structural tortuosity. Disordered pores are often caused by the crosslinking of certain polymer blocks, *e.g.*, PAN. While crosslinking is essential for PAN to maintain a high carbon yield, it inevitably limits the polymer chain mobility and leads to non-ideal block copolymer phases.[92] To obtain low-tortuosity morphologies such as ideal lamellae, various self-assembly and directed-assembly strategies are to be examined, such as solvent vapor annealing,[22,93] shear force-induced phase separation,[94,95] chemiepitaxy,[96–98] graphoepitaxy,[99,100] electric-field alignment,[101] and magnetic-field alignment,[102] which have achieved long-range order block copolymer lamellae. These methods have the potential to produce carbons with small ion diffusion resistances. Additionally, the effect of mesopores on the mechanical strength of porous carbon fibers remains unknown. Further investigations on the mechanical strength of porous carbon fibers are necessary. Potential structure-reinforcing strategies are to bundle porous carbon fibers with non-porous ones, or to develop carbon fibers of complex structures, such as the non-porous core and porous sheath.

Last but not least, collaboration between experimentalists and theorists can speed up the development of block copolymer based porous carbons for energy storage. Theory and simulations, *e.g.*, density functional theory,[103] can potentially predict the self-assembly of block copolymers under complex

conditions involving polymer compositions, processing methods, and guest molecules (*e.g.*, carbon precursors). Theoretical understanding of these parameters helps guide the design and synthesis of block copolymer-based porous carbons with well-controlled pore sizes, pore volumes, and surface areas. The emerging technique of inverse design,[104] which simulates starting materials based on end-product functionalities, will be instrumental in tailoring block copolymers with suitable compositions to derive porous carbons for specific applications. The persistent and collaborative efforts of practitioners from diverse disciplines will continue to propel the advancement of block copolymers in electrochemical energy storage.

Conflicts of interest

There are no conflicts to declare.

Acknowledgements

This article contains studies supported by the Air Force Office of Scientific Research under award number FA9550-17-1-0112, the National Science Foundation under Grant No. DMR-1752611, and the American Chemical Society Petroleum Research Foundation Doctoral New Investigator Award.

References

1 P. Simon, Y. Gogotsi and B. Dunn, *Science*, 2014, **343**, 1210–1211.
2 M. Salanne, B. Rotenberg, K. Naoi, K. Kaneko, P.-L. Taberna, C. P. Grey, B. Dunn and P. Simon, *Nat. Energy*, 2016, **1**, 16070.
3 M. Horn, J. MacLeod, M. Liu, J. Webb and N. Motta, *Econ. Anal. Policy*, 2019, **61**, 93–103.
4 L. G. H. Staaf, P. Lundgren and P. Enoksson, *Nano Energy*, 2014, **9**, 128–141.
5 X. J. He, X. J. Li, H. Ma, J. F. Han, H. Zhang, C. Yu, N. Xiao and J. S. Qiu, *J. Power Sources*, 2017, **340**, 183–191.
6 X. J. He, H. B. Zhang, H. Zhang, X. J. Li, N. Xiao and J. S. Qiu, *J. Mater. Chem. A*, 2014, **2**, 19633–19640.
7 H. Wang and L. Pilon, *J. Phys. Chem. C*, 2011, **115**, 16711–16719.
8 J. Yang, H. L. Wu, M. Zhu, W. J. Ren, Y. Lin, H. B. Chen and F. Pan, *Nano Energy*, 2017, **33**, 453–461.
9 T. Liu, F. Zhang, Y. Song and Y. Li, *J. Mater. Chem. A*, 2017, **5**, 17151–17173.
10 C. Zhong, Y. D. Deng, W. B. Hu, J. L. Qiao, L. Zhang and J. J. Zhang, *Chem. Soc. Rev.*, 2015, **44**, 7484–7539.
11 C. Yin, X. Liu, J. Wei, R. Tan, J. Zhou, M. Ouyang, H. Wang, S. J. Cooper, B. Wu, C. George and Q. Wang, *J. Mater. Chem. A*, 2019, **7**, 8826–8831.
12 T. Liu and G. Liu, *J. Phys.: Condens. Matter*, 2019, **31**, 233001.
13 K. Matyjaszewski, *Macromolecules*, 2012, **45**, 4015–4039.
14 D. J. Keddie, *Chem. Soc. Rev.*, 2014, **43**, 496–505.
15 A. Hirao, R. Goseki and T. Ishizone, *Macromolecules*, 2014, **47**, 1883–1905.
16 K. Satoh, Y. Mori and M. Kamigaito, *J. Polym. Sci. A*, 2019, **57**, 465–473.
17 C. W. Bielawski and R. H. Grubbs, *Prog. Polym. Sci.*, 2007, **32**, 1–29.
18 O. Altintas, M. Artar, G. t. Huurne, I. K. Voets, A. R. A. Palmans, C. Barner-Kowollik and E. W. Meijer, *Macromolecules*, 2015, **48**, 8921–8932.
19 M. Kopeć, R. Yuan, E. Gottlieb, C. M. R. Abreu, Y. Song, Z. Wang, J. F. J. Coelho, K. Matyjaszewski and T. Kowalewski, *Macromolecules*, 2017, **50**, 2759–2767.
20 K. Yan, L. B. Kong, Y. H. Dai, M. Shi, K. W. Shen, B. Hu, Y. C. Luo and L. Kang, *J. Mater. Chem. A*, 2015, **3**, 22781–22793.
21 H. Tian, Z. Lin, F. Xu, J. Zheng, X. Zhuang, Y. Mai and X. Feng, *Small*, 2016, **23**, 3155–3163.
22 Z. Zhou and G. Liu, *Small*, 2017, **13**, 1603107.
23 Y.-X. Tong, X.-M. Li, L.-J. Xie, F.-Y. Su, J.-P. Li, G.-H. Sun, Y.-D. Gao, N. Zhang, Q. Wei and C.-M. Chen, *Energy Storage Materials*, 2016, **3**, 140–148.
24 Z. Zhou, T. Liu, A. U. Khan and G. Liu, *Mol. Syst. Des. Eng.*, 2019, DOI: 10.1039/c1039me00066f.
25 J. Wang and S. Kaskel, *J. Mater. Chem.*, 2012, **22**, 23710–23725.
26 Y. Xia, Z. Yang and R. Mokaya, *Nanoscale*, 2010, **2**, 639–659.
27 X. Wu, L. Jiang, C. Long and Z. Fan, *Nano Energy*, 2015, **13**, 527–536.
28 C. Zhu, T. Liu, F. Qian, W. Chen, S. Chandrasekaran, B. Yao, Y. Song, E. B. Duoss, J. D. Kuntz, C. M. Spadaccini, M. A. Worsley and Y. Li, *Nano Today*, 2017, **15**, 107–120.
29 L. Jiang, J. Yan, R. Xue, G. Sun and B. Yi, *J. Solid State Electrochem.*, 2014, **18**, 2175–2182.
30 Z. Zhu, Y. Hu, H. Jiang and C. Li, *J. Power Sources*, 2014, **246**, 402–408.
31 Y. Song, S. Hu, X. Dong, Y. Wang, C. Wang and Y. Xia, *Electrochim. Acta*, 2014, **146**, 485–494.
32 A. Chen, Y. Yu, Y. Li, Y. Wang, Y. Li, S. Li and K. Xia, *J. Mater. Sci.*, 2016, **51**, 4601–4608.
33 M. Xie, K. Fang, Y. Shen, Y. Wang, J. Liang, L. Peng, X. Guo and W. Ding, *Microporous Mesoporous Mater.*, 2016, **223**, 114–120.
34 A. Sanchez-Sanchez, M. T. Izquierdo, J. Ghanbaja, G. Medjahdi, S. Mathieu, A. Celzard and V. Fierro, *J. Power Sources*, 2017, **344**, 15–24.
35 X.-Q. Zhang, A.-H. Lu, Q. Sun, X.-F. Yu, J.-Y. Chen and W.-C. Li, *ACS Appl. Energy Mater.*, 2018, **1**, 5999–6005.
36 A. Zhang, S. Cao, Y. Zhao, C. Zhang and A. Chen, *New J. Chem.*, 2018, **42**, 6903–6909.
37 S. Liu, X. Chen, X. Li, P. Huo, Y. Wang, L. Bai, W. Zhang, M. Niu and Z. Li, *RSC Adv.*, 2016, **6**, 89744–89756.
38 Y.-N. Sun, Z.-Y. Sui, X. Li, P.-W. Xiao, Z.-X. Wei and B.-H. Han, *ACS Appl. Nano Mater.*, 2018, **1**, 609–616.
39 D. Saha, Y. Li, Z. Bi, J. Chen, J. K. Keum, D. K. Hensley, H. A. Grappe, H. M. Meyer, S. Dai, M. P. Paranthaman and A. K. Naskar, *Langmuir*, 2014, **30**, 900–910.
40 M. Wu, P. Ai, M. Tan, B. Jiang, Y. Li, J. Zheng, W. Wu, Z. Li, Q. Zhang and X. He, *Chem. Eng. J.*, 2014, **245**, 166–172.

41 S. Wang, C. Han, J. Wang, J. Deng, M. Zhu, J. Yao, H. Li and Y. Wang, *Chem. Mater.*, 2014, **26**, 6872–6877.
42 Y. Hu, H. Liu, Q. Ke and J. Wang, *J. Mater. Chem. A*, 2014, **2**, 11753–11758.
43 Z. Lin, H. Tian, F. Xu, X. Yang, Y. Mai and X. Feng, *Polym. Chem.*, 2016, **7**, 2092–2098.
44 J. Tang, J. Liu, C. Li, Y. Li, M. O. Tade, S. Dai and Y. Yamauchi, *Angew. Chem., Int. Ed.*, 2015, **54**, 588–593.
45 Z. Tang, S. Liu, Z. Lu, X. Lin, B. Zheng, R. Liu, D. Wu and R. Fu, *Chem. Commun.*, 2017, **53**, 6764–6767.
46 S. Cao, T. Qu, A. Zhang, Y. Zhao and A. Chen, *ChemElectroChem*, 2019, **6**, 1696–1703.
47 R. Yuan, H. Wang, M. Sun, K. Damodaran, E. Gottlieb, M. Kopeć, K. Eckhart, S. Li, J. Whitacre, K. Matyjaszewski and T. Kowalewski, *ACS Appl. Nano Mater.*, 2019, **2**, 2467–2474.
48 K. Yan, L. B. Kong, K. W. Shen, Y. H. Dai, M. Shi, B. Hu, Y. C. Luo and L. Kang, *Appl. Surf. Sci.*, 2016, **364**, 850–861.
49 A. Zhang, A. Li, Y. Wang, M. Liu, H. Ma, Z. Song and J. Liu, *RSC Adv.*, 2016, **6**, 103843–103850.
50 Y. Wang, L.-B. Kong, X.-M. Li, F. Ran, Y.-C. Luo and L. Kang, *N. Carbon Mater.*, 2015, **30**, 302–309.
51 Y. Li, J. Dong, J. Zhang, X. Zhao, P. Yu, L. Jin and Q. Zhang, *Small*, 2015, **11**, 3476–3484.
52 D. K. Kim, N. D. Kim, S.-K. Park, K.-d. Seong, M. Hwang, N.-H. You and Y. Piao, *J. Power Sources*, 2018, **380**, 55–63.
53 J. Yang, G. Li, M. Cai, P. Pan, Z. Li, Y. Bao and Z. Chen, *Chem. Commun.*, 2017, **53**, 5028–5031.
54 K. Jost, G. Dion and Y. Gogotsi, *J. Mater. Chem. A*, 2014, **2**, 10776–10787.
55 Y. Dong, H. Lin, D. Zhou, H. Niu, Q. Jin and F. Qu, *Electrochim. Acta*, 2015, **159**, 116–123.
56 Z. Zhou, T. Liu, A. U. Khan and G. Liu, *Sci. Adv.*, 2019, **5**, eaau6852.
57 T. Liu, Z. Zhou, Y. Guo, D. Guo and G. Liu, *Nat. Commun.*, 2019, **10**, 675.
58 W. Dong, Z. Wang, Q. Zhang, M. Ravi, M. Yu, Y. Tan, Y. Liu, L. Kong, L. Kang and F. Ran, *J. Power Sources*, 2019, **419**, 137–147.
59 F. Ran, Y. Wu, M. Jiang, Y. Tan, Y. Liu, L. Kong, L. Kang and S. Chen, *Dalton Trans.*, 2018, **47**, 4128–4138.
60 J. L. Daristotle, O. M. Behrens, A. D. Sandler and P. Kofinas, *ACS Appl. Mater. Interfaces*, 2016, **8**, 34951–34963.
61 L. Persano, A. Camposeo, C. Tekmen and D. Pisignano, *Macromol. Mater. Eng.*, 2013, **298**, 504–520.
62 N. Bhardwaj and S. C. Kundu, *Biotechnol. Adv.*, 2010, **28**, 325–347.
63 E. Kang, G. Jeon and J. K. Kim, *Chem. Commun.*, 2013, **49**, 6406–6408.
64 C. Chen, Y. Zhang, Y. Li, J. Dai, J. Song, Y. Yao, Y. Gong, I. Kierzewski, J. Xie and L. Hu, *Energy Environ. Sci.*, 2017, **10**, 538–545.
65 Z. H. Huang, Y. Song, D. Y. Feng, Z. Sun, X. Sun and X. X. Liu, *ACS Nano*, 2018, **12**, 3557–3567.
66 K. Shi and K. P. Giapis, *ACS Appl. Energy Mater.*, 2018, **1**, 296–300.
67 K. Shi and I. Zhitomirsky, *ChemElectroChem*, 2015, **2**, 396–403.
68 L. Hu, W. Chen, X. Xie, N. Liu, Y. Yang, H. Wu, Y. Yao, M. Pasta, H. N. Alshareef and Y. Cui, *ACS Nano*, 2011, **5**, 8904–8913.
69 J. C. Lytle, J. M. Wallace, M. B. Sassin, A. J. Barrow, J. W. Long, J. L. Dysart, C. H. Renninger, M. P. Saunders, N. L. Brandell and D. R. Rolison, *Energy Environ. Sci.*, 2011, **4**, 1913–1925.
70 Y. X. Xu, Z. Y. Lin, X. Zhong, X. Q. Huang, N. O. Weiss, Y. Huang and X. F. Duan, *Nat. Commun.*, 2014, **5**, 4554.
71 M. Li and J. Xue, *J. Phys. Chem. C*, 2014, **118**, 2507–2517.
72 S. Zhu, H. Tian, N. Wang, B. Chen, Y. Mai and X. Feng, *Small*, 2018, **14**, 1702755.
73 Q. Ke, Y. Liu, H. Liu, Y. Zhang, Y. Hu and J. Wang, *RSC Adv.*, 2014, **4**, 26398–26406.
74 X. Xi, D. Wu, L. Han, Y. Yu, Y. Su, W. Tang and R. Liu, *ACS Nano*, 2018, **12**, 5436–5444.
75 L. Guo, X. Wang and Y. Wang, *Chem. Eng. J.*, 2017, **313**, 1295–1301.
76 D. Liu, G. Cheng, H. Zhao, C. Zeng, D. Qu, L. Xiao, H. Tang, Z. Deng, Y. Li and B.-L. Su, *Nano Energy*, 2016, **22**, 255–268.
77 M. J. Zhong, C. B. Tang, E. K. Kim, M. Kruk, E. B. Celer, M. Jaroniec, K. Matyjaszewski and T. Kowalewski, *Mater. Horiz.*, 2014, **1**, 121–124.
78 S. M. Bhaway, K. Kisslinger, L. Zhang, K. G. Yager, A. L. Schmitt, M. K. Mahanthappa, A. Karim and B. D. Vogt, *ACS Appl. Mater. Interfaces*, 2014, **6**, 19288–19298.
79 F. Ran, K. Shen, Y. Tan, B. Peng, S. Chen, W. Zhang, X. Niu, L. Kong and L. Kang, *J. Membr. Sci.*, 2016, **514**, 366–375.
80 Y. Zhou, S. L. Candelaria, Q. Liu, Y. Huang, E. Uchaker and G. Cao, *J. Mater. Chem. A*, 2014, **2**, 8472–8482.
81 B. You, P. Yin and L. An, *Small*, 2014, **10**, 4352–4361.
82 B. You, J. Jiang and S. Fan, *ACS Appl. Mater. Interfaces*, 2014, **6**, 15302–15308.
83 Y. Deng, A. Xu, W. Lu, Y. Yu, C. Fu and T. Shu, *New J. Chem.*, 2018, **42**, 7043–7048.
84 G. Hasegawa, K. Kanamori, T. Kiyomura, H. Kurata, T. Abe and K. Nakanishi, *Chem. Mater.*, 2016, **28**, 3944–3950.
85 L.-N. Han, X. Wei, Q.-C. Zhu, S.-M. Xu, K.-X. Wang and J.-S. Chen, *J. Mater. Chem. A*, 2016, **4**, 16698–16705.
86 J. Wang, J. Tang, B. Ding, V. Malgras, Z. Chang, X. Hao, Y. Wang, H. Dou, X. Zhang and Y. Yamauchi, *Nat. Commun.*, 2017, **8**, 15717.
87 H. Peng, B. Yao, X. Wei, T. Liu, T. Kou, P. Xiao, Y. Zhang and Y. Li, *Adv. Energy Mater.*, 2019, **9**, 1803665.
88 X. Liu, R. Mi, L. Yuan, F. Yang, Z. Fu, C. Wang and Y. Tang, *Front. Chem.*, 2018, **6**, 475.
89 Y. Liu, Z. Wang, W. Teng, H. Zhu, J. Wang, A. A. Elzatahry, D. Al-Dahyan, W. Li, Y. Deng and D. Zhao, *J. Mater. Chem. A*, 2018, **6**, 3162–3170.
90 J. G. Werner, G. G. Rodríguez-Calero, H. D. Abruña and U. Wiesner, *Energy Environ. Sci.*, 2018, **11**, 1261–1270.
91 T. Liu, T. Kou, D. Bulmahn, C. Ortuno-Quintana, G. Liu, J. Q. Lu and Y. Li, *ACS Appl. Energy Mater.*, 2018, **1**, 5043–5053.

92 J. D. Wilbur, E. D. Gomez, M. W. Ellsworth, B. A. Garetz and N. P. Balsara, *Macromolecules*, 2012, **45**, 7590–7598.
93 Z. Zhou, K. Cao, X. Chen, M. Nguyen, S. J. Talley, R. B. Moore, S. Martin and G. Liu, *Mol. Syst. Des. Eng.*, 2018, **3**, 357–363.
94 Z. Qiang, Y. Z. Zhang, Y. Wang, S. M. Bhaway, K. A. Cavicchi and B. D. Vogt, *Carbon*, 2015, **82**, 51–59.
95 Y. C. Kim, T. J. Shin, S.-M. Hur, S. J. Kwon and S. Y. Kim, *Sci. Adv.*, 2019, **5**, eaaw3974.
96 S. O. Kim, H. H. Solak, M. P. Stoykovich, N. J. Ferrier, J. J. de Pablo and P. F. Nealey, *Nature*, 2003, **424**, 411–414.
97 M. P. Stoykovich, M. Muller, S. O. Kim, H. H. Solak, E. W. Edwards, J. J. de Pablo and P. F. Nealey, *Science*, 2005, **308**, 1442–1446.
98 G. L. Liu, C. S. Thomas, G. S. W. Craig and P. F. Nealey, *Adv. Funct. Mater.*, 2010, **20**, 1251–1257.
99 I. Bita, J. K. W. Yang, Y. S. Jung, C. A. Ross, E. L. Thomas and K. K. Berggren, *Science*, 2008, **321**, 939–943.
100 K. G. A. Tavakkoli, K. W. Gotrik, A. F. Hannon, A. Alexander-Katz, C. A. Ross and K. K. Berggren, *Science*, 2012, **336**, 1294–1298.
101 V. Olszowka, M. Hund, V. Kuntermann, S. Scherdel, L. Tsarkova and A. Boker, *ACS Nano*, 2009, **3**, 1091–1096.
102 P. W. Majewski, M. Gopinadhan and C. O. Osuji, *J. Polym. Sci. Pol. Phys.*, 2012, **50**, 2–8.
103 X. He, X. Xie, J. Wang, X. Ma, Y. Xie, J. Gu, N. Xiao and J. Qiu, *Nanoscale*, 2019, **11**, 6610–6619.
104 K. R. Gadelrab, A. F. Hannon, C. A. Ross and A. Alexander-Katz, *Mol. Syst. Des. Eng.*, 2017, **2**, 539–548.